FISEVIER

Contents lists available at ScienceDirect

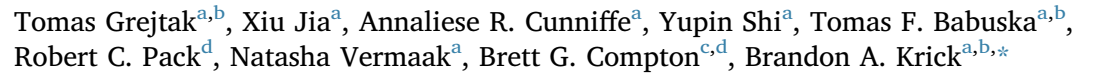
Additive Manufacturing

journal homepage: www.elsevier.com/locate/addma



Full Length Article

Whisker orientation controls wear of 3D-printed epoxy nanocomposites



- ^a Department of Mechanical Engineering and Mechanics, Lehigh University, Bethlehem, PA 18015, United States
- b Department of Mechanical Engineering, Florida A&M University- Florida State University College of Engineering, Tallahassee, FL 32310, United States
- ^c Mechanical, Aerospace, and Biomedical Engineering Department, University of Tennessee, Knoxville, TN 37996, United States
- ^d Materials Science and Engineering Department, University of Tennessee, Knoxville, TN 37996, United States



Keywords:
Additive manufacturing
Nanocomposites
Ceramic
Wear
Friction

ABSTRACT

Additive manufacturing enables design of multi-material composite materials with tunable mechanical properties. Previous studies on epoxy-based composites containing silica, clays or fiber showed that favorable mechanical properties can be achieved by controlling the fiber orientation and architecture. In this work the effect of the build direction and whiskers orientation on the wear properties of 3D printed epoxy-based nanocomposites is investigated. Epoxy-nanoclay-PTFE-SiC nanocomposites are fabricated using a direct-write additive manufacturing method that enables one to orient the SiC whiskers along the printing path. Tribological results show that variations in build direction and whiskers orientation relative to the sliding direction cause anisotropy in wear and friction in these nanocomposites. The best wear performance was achieved with the nanocomposites printed with whiskers oriented perpendicular to the sliding steel counter-surface and slid orthogonally to the build direction and print path orientation. All nanocomposites had significantly better wear properties than the unfilled epoxy sample. The results suggest that optimizing the whisker orientation and alignment in epoxy-based nanocomposites through direct-write additive manufacturing increases the wear performance. This enables an additional design paradigm when optimizing multifunctional, 3D-printed epoxy nanocomposites.

1. Introduction

Composite materials are widely used in many engineering applications and continue to replace traditional materials as they provide versatility and advanced mechanical properties that are not achievable by a single constituent material. In recent years, a lot of research effort has focused on polymer composites due to their favorable material properties and ability to replace some metal and ceramic materials in numerous engineering applications such as aerospace, automotive or electronics [1-5]. Engineers use various additives to further improve desirable mechanical properties of polymer composites. Fiber-reinforced polymer composites have become a very attractive additive due to an increasing demand for lightweight, stiff and strong multifunctional materials [1,3,6-8]. Nano-scale ceramic particles are very often used as fillers to further improve wear [9,10], strength [11,12], electrical [11] or thermal [13] properties of polymer composites. Progress in additive manufacturing (AM) has enabled the 3D printing of polymer composites with various fillers such as silicates or fibers [14-20]. The advantage of fabricating composites via AM instead of traditional methods such as molding or machining is that AM enables (i) the fast and precise building of complex structures of various materials and (ii) the control of mechanical properties with respect to print orientation [21,22]. Generally, the strength of the 3D printed materials is the highest when the applied load acts in the printing direction and the lowest when the material is loaded in the direction orthogonal to the printing path [23]. In material extrusion AM, this anisotropy arises due to weak layer-to-layer bonding, pores located between individual printed filaments, alignment of polymer chains, and alignment of nonspherical phases contained in the material.

The alignment and orientation of high-aspect-ratio particles suspended in flowing fluid has been studied extensively and has both theoretical and experimental support. For example, the seminal theoretical work of Jeffrey in 1922 showed that plate-like or rod-like ellipsoidal particles are expected to adopt a stable orientation with the long dimension of the particle aligned with the direction of extension in a purely extensional flow, while simple shear flow imposes periodic rotations on ellipsoidal particles, where they rotate rapidly when misoriented to the flow direction, and slowly when oriented with the flow

E-mail address: bkrick@fsu.edu (B.A. Krick).

^{*} Corresponding author at: Department of Mechanical Engineering, Florida A&M University - Florida State University College of Engineering, 2003 Levy Avenue Tallahassee, FL 32310, United States.

direction [24]. More recently, Folgar and Tucker [25] and Advani and Tucker [26] extended Jeffrey's theory to concentrated suspensions and to enable predictions of thermal and mechanical properties in short fiber composites based on flow history. These and similar models are now routinely used to predict mechanical properties in extruded and molded short fiber composites [27–30]. In the context of material extrusion AM, Shofner et al. showed that 100-nm-diameter carbon nanotubes align in the direction of printing for printed ABS polymer composites [31], Tekinalp et al. reported a high degree of fiber orientation in printed ABS/carbon fiber composites [32], and Gladman et al. elegantly demonstrated how alignment of nanofibrillated cellulose along the print direction can be utilized with swelling hydrogels to affect unique shape-morphing behavior in printed structures exclusively though control of anisotropic behavior associated with print path [33].

In addition, significant effort has focused on fabrication of epoxybased structural composites via material extrusion AM [19,20,34-36] as these composite systems have shown advanced combined mechanical, chemical and thermal properties [34,35,37-42]. Recently Raney and Compton demonstrated the 3D printing of carbon fiber- and silicon carbide (SiC) whisker-filled nanoclay-epoxy nanocomposites, which allows for control of the alignment of the fibers and whiskers [19,34]. These studies showed that the strength and stiffness of the composites are higher than that of the unfilled epoxy material [34], and that the strength and stiffness are considerably higher along the print direction compared to these properties transverse to the print direction. In addition, Raney and Compton showed that the orientation and arrangement of fibers within a single printed filament can be controlled through the use of a deposition nozzle with a rotational degree of freedom. In this approach, the ratio of rotation rate to translation rate dictates the orientation of fibers relative to the print direction, and rotation rate can be programmed during path planning to achieve spatially tailored fiber orientation patterns that would not be possible with any other fabrication method [19]. In another very recent study. Hmeidat et al. studied rheological and mechanical properties of 3D printed epoxy-based nanocomposites using four different filler combinations: nanoclay/SiC, nanoclay, fumed silica, and SiC/fumed silica [43]. The rheological studies showed that epoxy nanocomposites printed with nanoclay/SiC fillers have higher storage modulus, loss modulus, yield stress, flexural strength and modulus than other tested fillers. The mechanical testing also revealed that print path orientation and varying nozzle size and print speed causes anisotropy in flexural modulus and strength. Although the relationship between the strength properties, the fiber alignment, and print orientation of various 3D printed polymer composites has been studied, the wear properties are virtually unexplored. It is the particular interest of this research effort to investigate the wear performance and friction of polymer nanocomposites fabricated via AM as a function of print orientation and fiber alignment.

Literature provides several studies on the wear properties of polymer composite materials relative to their fiber orientation ranging from natural fibers [44–46] to ceramic fibers [47–49]. The studies of Sung [47] and Chin [45] showed that the lowest wear and highest friction was achieved with the composite samples that were tested with fibers oriented perpendicular to the counter surface. However, none of these studies focused on 3D printed samples of polymer

nanocomposites. In this work, the effect of the whisker orientation and overall build direction on the wear properties of 3D printed polymer nanocomposites is investigated. The studied polymer nanocomposites are composed of epoxy-nanoclay-PTFE-SiC and fabricated using direct write (DW) additive manufacturing, which allows control of the SiC whisker spacing and orientation [19,34].

In the current work, the effect of the build direction and whisker orientation on the wear properties of these 3D printed epoxy-based nanocomposites is investigated by testing the samples printed with normal (perpendicular), parallel and transverse whisker orientation relative to the counter-surface and sliding direction. The comprehensive wear testing includes measurements of wear rates, volume loss, friction and analysis of the worn sliding surfaces of the nanocomposites as well as wear rates of the steel counter-surfaces. The tribological results are analyzed and used to explain the wear mechanism that drives the differences in the wear performance due to variations in printing and whisker orientation relative to the sliding direction and counter-surface.

2. Materials and methods

2.1. 3D printed composite specimens

Epoxy-based inks were formulated by first mixing 1 g of 1-ethyl-4methylimidazolium dicyanamide (BASF Basionics VS 03, obtained from Sigma-Aldrich, Inc., St. Louise, MO) into 20 g of epoxy resin (Epon 826 Hexion Inc., Columbus, OH) using a centrifugal planetary SpeedMixer (Flacktek Inc., Landrum, SC) at 1700 rpm for 1 min under vacuum of 0.1 atm. Next, 10.75 g of SiC microfibers (SI-TUFF SF-1, Haydale Technologies, Greer, SC) were added to the resin, followed by 1.55 g of nanoclay (Garamite 7305, BYK Chemie GmbH, Wesel, Germany), and 2.58 g of PTFE micropowder (Microdisperse-3000, Polysciences, Inc. Warrington, PA). The final composition contained 73 vol.% epoxy, 14.3 vol.% SiC, 5 vol.% PTFE, 4.1 vol.% nanoclay and 3.6 vol.% curing agent, Table 1. This formulation is based on the formulation initially developed by Compton and Lewis [34] for 3D-printing of lightweight, high stiffness epoxy composites and refined by Hmeidat et al. [43]. The SiC whiskers impart high strength and stiffness to the final composite, while the use of nanoclay in these formulations is instrumental to achieving sufficient shear thinning and yield stress behavior in the ink rheological properties that are critical for successful extrusion-based 3D printing [20,34,35,43]. PTFE microparticles were chosen to impart lubricity to the composite and reduce noise during wear testing. The ink was mixed at 1800 rpm for two minutes after the addition of each

After mixing, the ink was loaded into a 10cc syringe barrel (Nordson EFD, Westlake, OH) using a spatula and centrifuged at 3900 rpm for 5 min using a Sorvall ST-8 Centrifuge (ThermoFisher Scientific, Waltham, MA) to remove any entrained air from the loading process. The filled syringe barrel was then mounted on a three-axis gantry (Shopbot Tools, Inc, Durham, NC) inside a 4x pressure multiplier (HP10cc, Nordson EFD) and connected to a pneumatic control system comprised of a voltage-controlled pressure regulator and solenoid valves. Samples were printed onto PTFE-coated aluminum foil (Bytac, Saint Gobain Performance Plastics, Worcester, MA) at 25 mm/s using 90 psi (620.5 kPa) supply pressure $(90 \times 4 = 360 \text{ psi applied to the})$

Table 1
Composition of epoxy-nanoclay-PTFE-SiC nanocomposites samples.

Constituent	Form	Density (g/cm ³)	Mass (g)	Weight fraction	Volume fraction
Epon 826	Liquid	1.16	20	0.557	0.73
VS 03	Liquid	1.06	1	0.028	0.036
Nanoclay	~ 6 µm agglomerates of nanoplatelets	1.60	1.55	0.043	0.041
SiC whiskers	0.65-μm-diameter rods, 10-12 μm average length	3.21	10.75	0.30	0.143
PTFE	3 μm powder	2.25	2.58	0.072	0.050

ink). A double tapered luer-lock deposition nozzle (Fisnar, Germantown, WI) was used with outlet diameter of 0.84 mm. The layer height was set at 0.554 mm, and the road-to-road spacing was set to 0.714 mm. Simple rectilinear raster patterns were programed in g-code using Scilab software (Scilab Enterprises, Institut National de Recherche en Informatique et en Automatique, Rocquencourt, France) and used to print unidirectional blocks 42 mm x 21 mm x 9 mm.

Unfilled epoxy samples were prepared from the same epoxy/curing agent blend without the addition of SiC, nanoclay or PTFE. Thick discs (~ 10 mm thick, 20 mm in diameter) were cast in sample mounting cups. All samples were cured at 100 °C for 15 h followed by two hours at 220 °C.

The samples were cut and machined into rectangles with dimensions of $6.3\,\mathrm{mm} \times 6.3\,\mathrm{mm} \times 12.0\,\mathrm{mm}$ using a low-speed diamond saw milling machine. The testing surface of the samples was machined flat to ensure flat-on-flat contact between the sample and the counter surface. Four test specimens were machined, each with a different nominal whisker orientation, see Section 2.3 Experiment Design. All samples were sonicated in methanol to prevent contamination of the surface from machining.

The counter-surfaces were 304 L stainless steel coupons with a lapped finish (Metal Samples Company-Alabama Specialty Products Inc, Munford, AL) and with dimensions of 38 mm x 25 mm x 3.7 mm and average surface roughness of ~ 150 nm. The counter-surfaces were rinsed in methanol and dried prior to wear testing. All wear tests were performed in lab air at room temperature and average humidity conditions.

2.2. Tribological measurements

Flat-on-flat, linear reciprocating wear experiments, Fig. 1a, were conducted on a 4-station tribometer; this enables simultaneous wear measurements on four specimens in the same environment. The test specimen was loaded against the counter surface at a normal load of $\sim 150\,\mathrm{N}$ ($\sim 3.8\,\mathrm{MPa}$ contact pressure - note: design considerations using polymer-based solid lubricants enable significantly larger contact area than those in traditional rolling element bearings) and slid in a reciprocating fashion at the sliding speed of 50 mm/s where the length of one sliding stroke was 25 mm. Forward and reverse sliding stroke results in one sliding cycle. The wear experiments were conducted for a total of 500 K sliding cycles (25.4 km) and the specimen mass was measured after 1 K, 4 K, 5 K, 10 K, 10 K, 20 K, 50 K, 100 K, 100 K and 200 K sliding cycles. The mass of the specimens was recorded using a laboratory scale (Mettler Toledo XS205DU) with a $1\times10^{-5}\,\mathrm{g}$

resolution. Normal and frictional forces were measured using straingauge-based load cells. The steel counter-surfaces were mounted on the reciprocating linear stage while the epoxy-based samples were mounted on the stationary load cell. Control of applied load, linear stage and data acquisition was performed using MATLAB (Natick, MA, USA).

Wear rate was measured based on change in a specimen's volume as a function of increasing sliding cycles. The initial volume, $V \, (\text{mm}^3)$, of the sample was determined by measuring its length, width and thickness. The density, $\rho \, (\text{mg/mm}^3)$, of the sample was measured as its initial mass, $m \, (\text{mg})$, divided by the initial volume, V. The change in volume or wear volume, $V_{worn} \, (\text{mm}^3)$, of the nanocomposites was determined as a change in its mass, $\Delta m \, (\text{mg})$, divided by its density:

$$V_{worn} = \frac{\Delta m}{\rho} \tag{1}$$

The wear rate, K (mm³/Nm), was then calculated as the worn volume, V_{worn} , divided by the applied normal force, F_n (N), times the sliding distance, d (m):

$$K = \frac{V_{worn}}{F_n d} \tag{2}$$

A Monte Carlo technique was used to calculate the steady-state wear rates, K_{ss} (mm³/Nm), and its uncertainties as described in Schmitz et al. [50] (not to be confused with kinetic Monte Carlo simulations for materials modeling [51,52]). Here, the measurement uncertainties in normal force, F_{ns} , sliding distance, d, and wear volume, V_{worn} , were used to generate 100,000 different scenarios for the measured wear volume, normal force and sliding distance. Steady-state wear rate (mean) and its uncertainties (standard deviation) are then determined as a slope of V_{worn} vs F_nd (Eq. 2) by fitting the last three data points (last 300,000 sliding cycles of total 500,000 sliding cycles if the sample did not fail prematurely due to high wear or friction).

The incremental wear rate, K_{incr} (mm³/Nm), was calculated as an instantaneous change in worn volume over a single wear experiment, i:

$$K_{incr} = \frac{V_{worn}(i+1) - V_{worn(i)}}{(F_n d)_{(i+1)} - (F_n d)_{(i)}}$$
(3)

Friction coefficients were calculated by averaging the middle 50 % of the forward and reverse data of each reciprocating stroke as frictional force over normal force [53]. The average friction coefficient of each tested sample is determined as the mean value of friction coefficients of all tested cycles. The wear rate of the steel counter surfaces, K_{cs} (mm³/Nm), was determined from the wear tracks after 500,000 sliding cycles. The worn surface profile, Fig. 1b, was measured with scanning

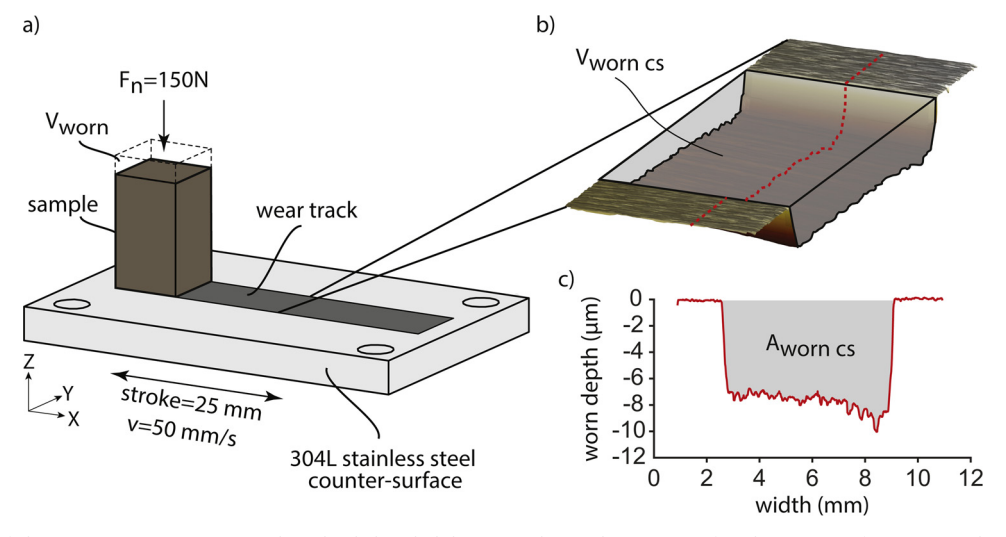


Fig. 1. a) Schematic of the wear experiment. A sample is loaded and slid against the steel counter-surface b) Worn surface topography of the counter-surface measured with optical profilometry. c) Wear rate, K_{cs} , calculated from the worn surface area, $A_{worn\ cs}$, which is the cross-section of the wear track as highlighted in b).

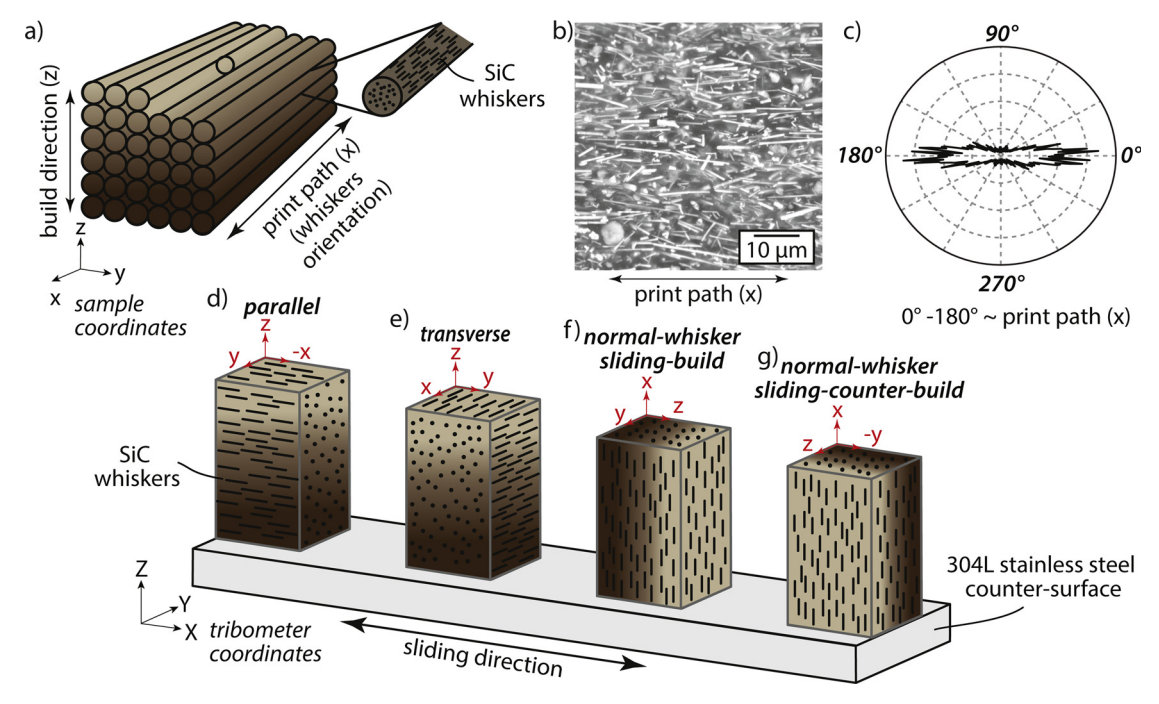


Fig. 2. a) Schematic of printing epoxy-nanoclay-PTFE-SiC nanocomposite samples using direct write 3D-printing. b) SEM image of the nanocomposite. c) Orientation distribution of whiskers. d–g) Four samples used in wear testing, each with different whiskers orientation relative to the counter-surface and sliding direction. Color gradient and x-y-z coordinates correspond to the reference sample in a). d) Parallel. e) Transverse. f) Normal-whisker, sliding-build. g) Normal-whisker, sliding-counter-build.

white-light interferometry (Contour GT; Bruker, Billerica, MA). The wear rate was calculated from the average measured cross sectional worn area, A_{worn} , Fig. 1c, divided by the applied normal force, F_n , times the number of total sliding passes (two times total sliding cycles, n) [54]:

$$K_{cs} = \frac{V_{worn}}{F_n d} \left[\frac{mm^3}{Nm} \right] = \frac{A_{worn} [mm^2] s [m] 1000 \left[\frac{mm}{m} \right]}{2n [cycles] s \left[\frac{m}{cycles} \right] F_n [N]} = \frac{1000}{2} \frac{A_{worn}}{nF_n}$$
(4)

where s = stroke per sliding pass (half a sliding cycle).

Photograph images of the sliding surfaces of the nanocomposites, Fig. 5, were taken using a document camera (Ipevo CDVU-03IP, Sunnyvale, CA).

2.3. Experiment design

The effect of the whiskers orientation on the wear properties of epoxy-nanoclay-PTFE-SiC nanocomposites were studied using four samples with varying whiskers orientation relative to the steel countersurface and the direction of sliding, Fig. 2. The sample nomenclature is defined based on how the sample (x-y-z coordinate system; where the x-axis is the SiC whiskers orientation and the z-axis is the build direction, Fig. 2a) is oriented relative to the tribometer (X-Y-Z coordinate system, where the X-axis is the friction force direction and the Z-axis is the normal force direction). Naming conventions are as follows:

- "parallel" (Fig. 2d)
 - o Contact orientation: print build direction plane (normal to sample z-axis) in contact (z aligned with Z).
 - o Sliding direction: slide along whiskers and print path orientation (sample x-axis along tribometer X-axis).
- "transverse" (Fig. 2e)
- o Contact orientation: print build direction plane (normal to sample z-axis) in contact (z aligned with Z).
- o Sliding direction: slide across whiskers and print path orientation (sample y-axis along tribometer X-axis).

- "normal-whisker, sliding-build" (Fig. 2f)
 - o Contact orientation: whiskers and print path orientation plane (sample x-axis) in contact (sample x aligned with tribometer Z).
 - o Sliding direction: slide in the build direction (sample z-axis); along tribometer X-axis.
- "normal-whisker, sliding-counter-build" (Fig. 2g)
 - o Contact orientation: whiskers and print path orientation plane (sample x-axis) in contact (sample x aligned with tribometer Z).
 - o Sliding direction: slide across the build direction (sample y-axis); along tribometer X-axis.

SEM imaging (Phenom, Nanoscience Instruments INC, Phoenix, AZ) was performed on the filament surface of epoxy-nanoclay-PTFE-SiC nanocomposite sample, showing that whiskers are aligned along the print path direction, Fig. 2b. The orientation distribution of the whisker was obtained using an image-based fiber orientation calculator based on Fourier transform methods as outlined in Sander and Barocas [55]. Results show that the whiskers are aligned along 0° and 180°, the print path direction, Fig. 2c.

3. Results

The wear properties of epoxy-nanoclay-PTFE-SiC nanocomposites showed dependence on the orientation of SiC whiskers and build direction relative to the sliding direction and the steel counter-surface. The anisotropic wear behavior was observed in the wear volume, steady-state wear rate, friction coefficient and wear of the steel counter-surface, Figs. 3,4 Table 2. The normal-whisker, sliding-counter-build nanocomposite had better wear properties than the normal-whisker, sliding-build, parallel and transverse nanocomposites. The normal-whisker, sliding-counter-build sample had the lowest steady-state wear rate, $\sim 3.27 \times 10^{-6}~\text{mm}^3/\text{Nm}$, of all tested composite samples, Fig. 3b. The normal-whisker, build sliding, parallel and transverse samples had very similar steady-state wear rates, which are 25–34 % higher than the normal-whisker, sliding-counter-build sample with the lowest wear. The unfilled epoxy sample broke after 200 K sliding cycles most likely

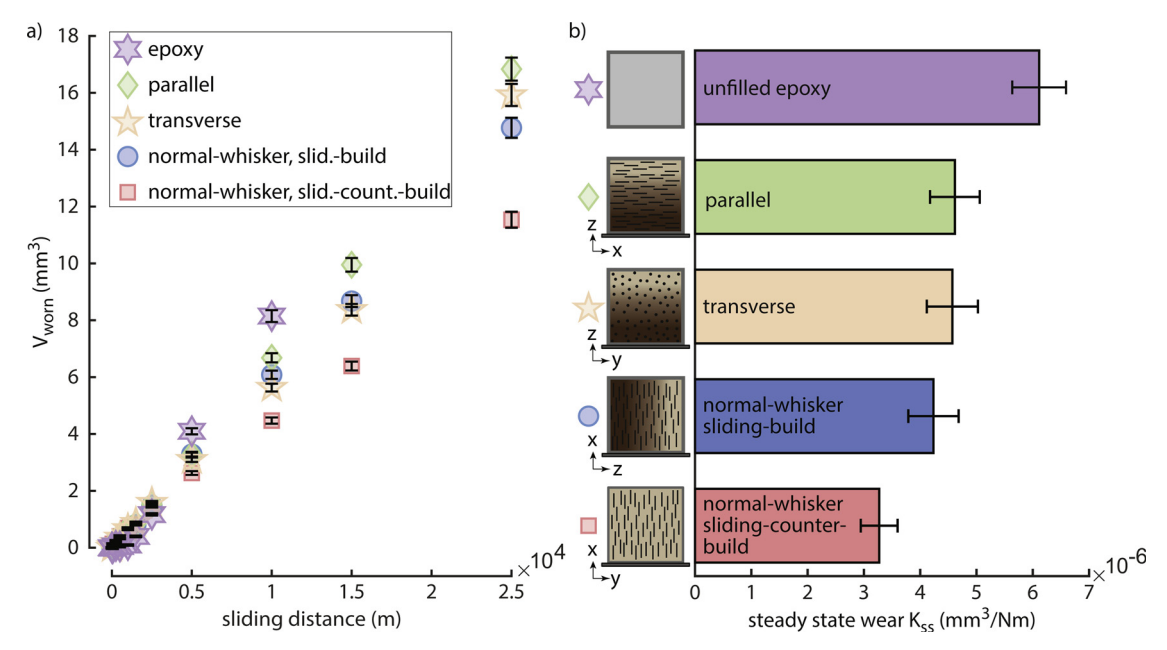


Fig. 3. Wear experiments results. a) Wear volume vs sliding distance for all four tested nanocomposites and unfilled epoxy sample. The normal-whisker, sliding-counter-build nanocomposite had the lowest wear volume. The unfilled epoxy sample had the highest wear volume of all, however, the sample failed after 200 K sliding cycles. b) Steady-state wear rate determined using Monte Carlo technique.

due to high friction, Fig. 4a. The steady-state wear rate of the unfilled epoxy sample at the last measured experiment (200 K sliding cycles) was the highest among all tested samples $\sim\!6.11\times10^{-6}\,\text{mm}^3/\text{Nm}$. The trends in the wear volume, Fig. 3a, correspond with the trends in the steady state wear rates.

Tribological measurements showed interesting correlation between the wear rates and friction coefficients of nanocomposite samples, Fig. 4a. Although the differences in friction coefficients are small, the trends are inversely proportional to the measured wear rates. The normal-whisker, sliding-counter-build sample had the lowest wear rate; however, the average friction coefficient, $\mu_{average}$, was the highest of all, ~ 0.57 . The parallel and transverse samples had the lowest friction of all composite samples, ~ 0.50 , even though their steady-state wear rates were the highest, Fig. 4a, Table 2. The unfilled epoxy sample had an excessively high friction coefficient, ~ 0.75 , which probably caused a failure of the sample after 200 K sliding cycles.

The measured wear rates of the steel counter-surfaces showed similar trends as the wear rates of the nanocomposite samples, Fig. 4b. The counter-surface that was used for the lowest wear specimen, normal-whisker, sliding-counter-build, had the lowest wear of all counter-surfaces, $\sim\!1.71\times10^{-7}\,\mathrm{mm^3/Nm}$. Parallel specimen, which was among the highest wear nanocomposites, wore the steel counter-surface significantly more than the other nanocomposite specimens. The wear rate of this steel counter-surface was $\sim\!2.75\times10^{-7}\,\mathrm{mm^3/Nm}$ which is $\sim\!47$ % higher than the counter-surface used for normal-whisker, sliding-counter-build sample. The unfilled epoxy sample did not cause wear of the counter-surface.

Comparison of the sliding surface of all nanocomposites before and after the wear testing is shown in Fig. 5. Initially (0 cycles), the sliding surface of the nanocomposite samples is machined flat to ensure an even unworn surface. The initial surfaces of normal-whisker, sliding-build and normal-whisker, sliding-counter-build samples have several

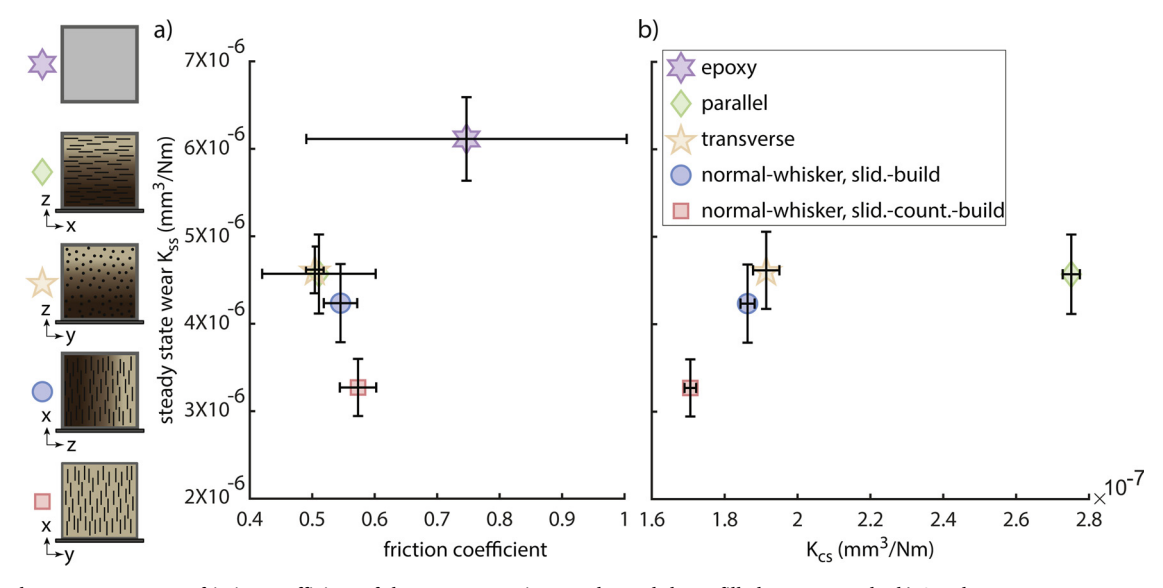


Fig. 4. a) Steady-state wear rate vs friction coefficient of the nanocomposite samples and the unfilled epoxy sample. b) Steady-state wear rate vs wear rate of the counter surfaces excluding the unfilled epoxy sample because it did not wear the steel counter-surface.

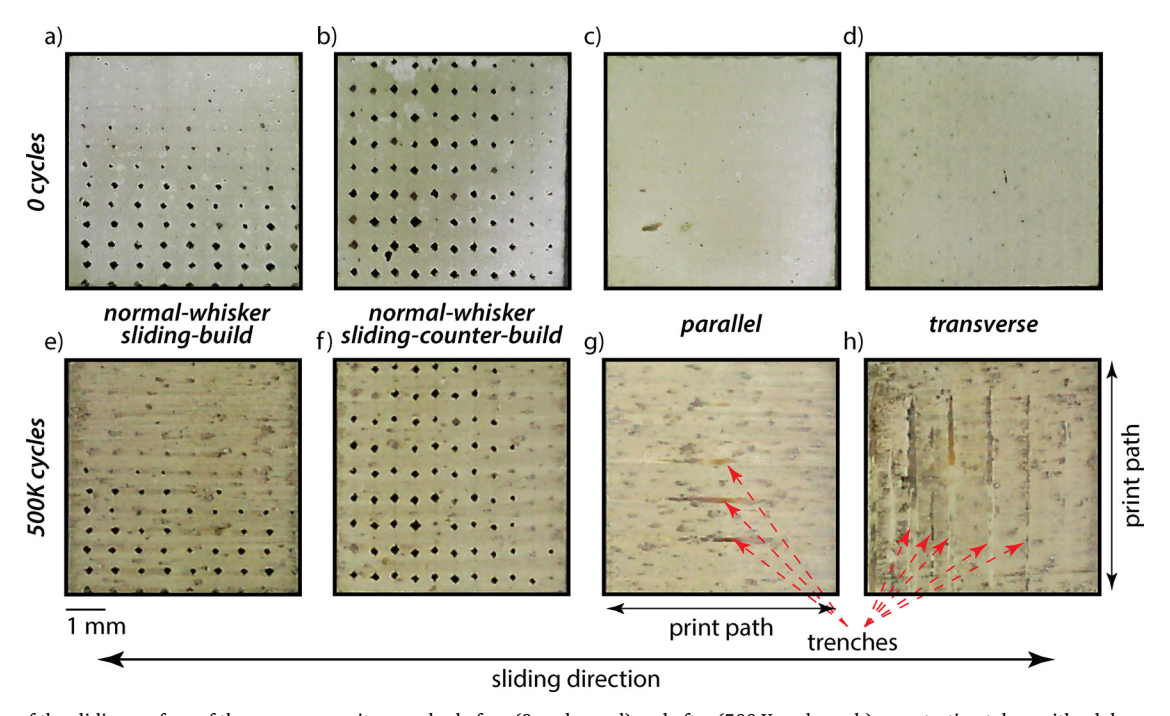


Fig. 5. Images of the sliding surface of the nanocomposite samples before (0 cycles; a-d) and after (500 K cycles; e-h) wear testing taken with a lab camera. Images of the unworn normal-whisker, sliding-build (a) and normal-whisker, sliding-counter-build (b) surfaces show several micro voids as a result of 3D printing. The parallel (c) and transverse (d) composite samples started with smooth surfaces without any apparent voids. The sliding surfaces of normal-whisker, sliding-build (e) and normal-whisker, sliding-counter-build (f) samples after 500 K sliding cycles show apparent wear debris and third-body tribofilms. The images of the samples with whiskers oriented in the parallel (g) and transverse (h) direction after 500 K sliding cycles show damage and emergence of trenches on the surface.

microvoids due to the 3D printing technique, Fig. 5a,b. The initial surfaces of the parallel and transverse nanocomposites are smooth and flat. Fig. 5c,d. The worn sliding surfaces (after 500 K sliding cycles) of normal-whisker, sliding-build and normal-whisker, sliding-counterbuild samples are covered with wear debris, with streaks of third bodies aligned with the sliding direction, Fig. 5e,f. The sliding surfaces of the parallel and transverse composites after 500 K sliding cycles show trenches, which follow the print path direction, likely corresponding to voids between the print filaments (Fig. 5g,h). The trenches appears to be more pronounced in the transverse nanocomposite, with some evidence of onset of delamination, Fig. 5h.

4. Discussion

The results demonstrate that whisker orientation relative to the sliding direction causes anisotropic wear behavior of the AM fabricated nanocomposites and that the differences in the wear properties are related to the whiskers topography at the sliding interface. The surface interaction between the sliding contact of the nanocomposite and the steel counter-surface has a direct influence on the wear properties because in the wear of fiber polymer composites the matrix wears first, followed by fiber wear, fiber fracture and detachment of fibers from the matrix [46,56]. This order of the wear process can be observed in the incremental wear plot, Fig. 6. Initially, all nanocomposites have higher wear rates due to a combined wear of the whiskers and polymer matrix.

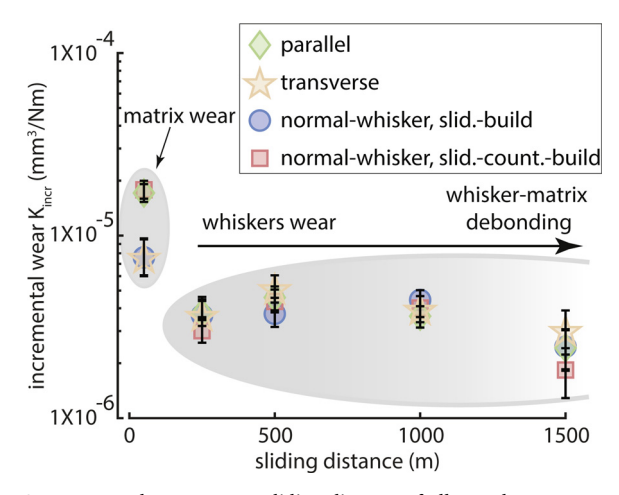


Fig. 6. Incremental wear rate vs sliding distance of all tested nanocomposites indicating a possible transition from matrix dominated wear to more whiskers dominated wear and debonding of whiskers from the polymer matrix.

After the initial thin layer of the matrix is worn, the incremental wear rate drops because the wear is dominated by the stiff and wear resistant SiC whiskers which can cause increased wear of the steel counter-surface. At this stage, the load is carried by the whiskers which could lead

Table 2
Summary of steady-state wear rate and friction coefficient of the nanocomposites and epoxy and wear rate of the steel counter-surfaces.

Orientation Of Whiskers	$K_{ss} (mm^3N^{-1}m^{-1})$	$K_{ss (uncertainty)} (mm^3N^{-1}m^{-1})$	$\mu_{average}$	$K_{cs} (mm^3N^{-1} m^{-1})$	K _{cs (uncertainty)} (mm ³ N ⁻¹ m ⁻¹)
Normal-whisker sliding-build Normal-whisker Sliding-counter-build Parallel Transverse Epoxy	4.24×10^{-6} 3.27×10^{-6} 4.61×10^{-6} 4.57×10^{-6} 6.11×10^{-6}	4.47×10^{-7} 3.27×10^{-7} 4.41×10^{-7} 4.54×10^{-7} 4.78×10^{-7}	0.55 0.57 0.51 0.50 0.75	1.86×10^{-7} 1.71×10^{-7} 2.75×10^{-7} 1.91×10^{-7}	1.93×10^{-9} 1.59×10^{-9} 2.35×10^{-9} 3.62×10^{-9}

Additive Manufacturing 36 (2020) 101515

to possible whisker failure and debonding from the polymer matrix with increasing sliding cycles. The whiskers do not debond from the matrix if the adhesion between the whiskers and the matrix is stronger than the shear force acting on the interface; in this case, the whiskers could break or fracture if the friction-induced load on the fiber exceeds a critical load. If the interfacial adhesion cannot resist the shear force, the whiskers detach from the polymer matrix. Whisker failure or detachment decreases the strength of the sliding surface and the epoxy polymer begins to dominate the sliding interface which leads to a decrease in the wear resistance of the nanocomposite.

Crack propagation due to the microstructure and cyclic load also plays a role in the wear properties of these 3D printed nanocomposites. Generally, cracks initiate under the sliding surface and increase with increasing sliding cycles [57,58]; these cracks then run along the whisker-matrix boundary and weak interfaces, they can cause debonding of the whiskers from the polymer matrix and delamination of the sliding surface which further enhances the wear of the epoxy nanocomposites.

The tribological testing showed that the wear rates of the epoxynanoclay-PTFE-SiC nanocomposites are improved when the whiskers are oriented normal to the steel counter-surface and sliding direction, Fig. 3. This relationship between wear and the whiskers orientation in the epoxy matrix is consistent with the previous studies on kenaf fiberepoxy in the work of Chin [45], sisal fiber-epoxy in Chand [46] and graphite fiber-epoxy and Kevlar fiber-epoxy in Sung [47]. The difference between parallel and transverse samples was minimal, ~ 0.9 %. The studies showed that the trends in the wear resistance between parallel and transverse sliding are inconsistent and depend on the type of fiber/whisker [45-47]. In parallel and transverse samples whisker debonding increases because the larger contact area of the whiskers is in the sliding contact with the steel counter-surface. Long areas of the fiber are exposed as the matrix around it wears. Detachment of whiskers is more difficult in normal-whisker, sliding-build and normal-whisker, sliding-counter-build nanocomposites because their whiskers are embedded in the matrix and only the tips are in contact with the sliding surface. Cracks that nucleate under the sliding surface due to high contact stresses and run along the print filaments and whisker-matrix interface, have a bigger impact on the wear in the parallel and transverse samples because their print filaments and whiskers are oriented along the counter-surface and are slid either along the print path (parallel sample) or across the print path (transverse sample) direction. We hypothesize that this crack propagation has a lower effect on the wear and emergence of trenches in the normal-whisker, sliding-build and normal-whisker, sliding-counter-build nanocomposites because the cracks run perpendicularly (out of plane) with respect to the countersurface and sliding. Interestingly, the normal-whisker, sliding-counterbuild sample has shown a higher wear resistance than the normalwhisker, sliding-build sample. The boundaries between the printed layers of the epoxy nanocomposites form weak interfaces. In the normal-whisker, sliding-build sample, the sliding is across these weak interfaces. The stresses due to the reciprocating cycles cause opening and closing of these weak interfaces which could lead to a lower wear

In the parallel and transverse samples, the interfacial adhesion between the whiskers and the polymer matrix could not withstand the large, friction-induced shear stresses, aligned with the whiskers. We hypothesize this resulted in debonding of the whiskers from the matrix and led to an emergence of trenches and higher wear rates. The trench patterns in the transverse sample, Fig. 5h, are in the print path direction which suggests that the boundaries between these print paths could also serve as weak interfaces and the cracks caused by reciprocating stresses ran along that direction, eventually resulting in large-scale trenches/wear of a print filament. Kemp et al. [59] in their work on 3D printed boron nitride polysilazane ceramic composites suggested that the printing-related voids could cause anisotropy. These voids, Fig. 5a,b, are aligned with the direction of the print path, therefore could weaken

the sliding surfaces in parallel and transverse nanocomposites. The reciprocating stresses do not seem to cause whisker debonding in the normal-whisker, sliding-build and normal-whisker, sliding-counterbuild samples which suggests that the normal orientation of the whiskers relative to the counter-surface and sliding provides the greatest wear resistance. All tested nanocomposites show higher wear resistance and lower friction than the unfilled epoxy.

Measured friction coefficients of the epoxy-nanoclay-PTFE-SiC nanocomposites showed counter-intuitive trends as the lowest friction was achieved with the higher wear composites and highest friction with the most wear resistant composite, Fig. 4a. Similar counter-intuitive friction results were found in previous studies [45,47]. These results suggest the importance of micromechanics at the sliding interface of the nanocomposites and the steel counter-surface. In normal-whisker, sliding-build and normal-whisker, sliding-counter-build nanocomposites, whiskers do not detach from the polymer matrix and dominate the wear performance. The contact area between the whiskers and the steel counter-surface is very small because only the tips of the whiskers are in the sliding contact. This hard asperity contact results in high contact stresses and abrasive ploughing wear in which friction increases. The contact stresses between the SiC whiskers and the steel counter-surface in the parallel and transverse nanocomposites are smaller due to a larger sliding contact area of the SiC whiskers. The whiskers debonding from the polymer matrix is easier and enhances wear. A formation of third bodies from the wear debris between the sliding interface of the nanocomposite and steel counter-surface reduces the hard, abrasive contact and lowers the friction. The friction coefficient of the unfilled epoxy sample was the highest of all tested samples which most likely resulted in the premature failure of the sample - catastrophic fracture of the sample in two consecutive experiments.

Although the difference in the wear rates and friction coefficients between the parallel and transverse nanocomposites were minimal, the differences in the wear of the counter-surfaces are more obvious. In the parallel nanocomposite, the whiskers are oriented along the sliding direction which allows them to slide along the projected cross-section area and form consistent wear patterns on the steel counter-surface that increase in depth with increasing sliding cycles. The wear rate of the steel counter-surface used for transverse nanocomposites is lower because the whiskers are oriented in the counter-sliding direction which does not allow the formation of constant wear patterns. The wear of the counter-surface is lowered by the polymer matrix between the whiskers that provides a softer lubricating contact. The lowest wear rate of the steel counter-surface was achieved with the normal-whisker, slidingcounter-build nanocomposite. This whisker arrangement offers the lowest sliding contact area of whiskers on average and the lowest formation of polymer wear debris, which lowers the abrasive wear of the steel counter-surface. Future work, including detailed microscopy studies of the sliding surfaces as well as systematic studies on composition and fiber surface functionalization to assess effects of the fiber-matrix interface could provide valuable insight into the wear mechanism of the 3D printed nanocomposites with controlled filler orientations.

5. Conclusions

Tribological experiments were performed on 3D printed epoxy-nanoclay-PTFE-SiC nanocomposites to explore the influence of the SiC whiskers orientation and build direction on their wear properties. The wear rate, friction coefficient as well as the wear rate of the steel counter-surface of these epoxy nanocomposites were measured in four different whisker arrangements with respect to the steel counter-surface and sliding: normal-whisker, sliding-build and normal-whisker, slidingcounter-build, parallel and transverse. The unfilled epoxy-based sample was also tested. The tribological testing showed anisotropic wear properties of these nanocomposites as a function of the whisker orientation and build direction. The normal-whisker, sliding-counterbuild nanocomposite had the highest wear resistance and the lowest

wear of the steel counter-surface among all tested nanocomposites. Although this nanocomposite had the highest friction, its wear rate is ~25-34 % lower than the normal-whisker, build sliding, parallel and transverse nanocomposites. The debonding of the whiskers from the polymer matrix is easier in the transverse and parallel samples which results in weakening of the sliding surfaces and higher wear. The whisker detachment is more difficult in the normal-whisker, slidingbuild and normal-whisker, sliding-counter-build nanocomposites because the whiskers are bonded into the polymer matrix and only the tips are exposed to the sliding surface. The lowest wear rate was achieved in the normal-whisker, sliding-counter-build nanocomposite due to the sliding occurring along the weak interfaces formed by the print layers. The parallel nanocomposite wore the steel counter-surface ~ 47 % more than the normal-whisker, sliding-counter-build nanocomposite. The parallel whisker alignment allows sliding of these hard asperities with larger contact area along the projected area and with constant wear patterns. The normal-whisker, sliding-counter-build nanocomposite wears the steel counter-surface the least because the hard SiC whiskers have the smallest interfacial contact area.

CRediT authorship contribution statement

Tomas Grejtak: Conceptualization, Methodology, Software, Validation, Formal analysis, Investigation, Resources, Data curation, Writing - original draft, Visualization. Xiu Jia: Conceptualization, Methodology, Writing - review & editing. Annaliese R. Cunniffe: Investigation, Data curation. Yupin Shi: Investigation, Data curation. Tomas F. Babuska: Methodology, Software, Validation, Formal analysis, Investigation, Resources, Writing - review & editing, Visualization. Robert C. Pack: Investigation, Resources, Data curation. Natasha Vermaak: Conceptualization, Methodology, Validation, Formal analysis, Resources, Writing - review & editing, Supervision, Project administration, Funding acquisition. Brett G. Compton: Conceptualization, Methodology, Software, Validation, Formal analysis, Investigation, Resources, Data curation, Writing - review & editing, Funding acquisition. Brandon A. Krick: Conceptualization, Methodology, Software, Validation, Formal analysis, Investigation, Resources, Writing - review & editing, Visualization, Supervision, Project administration, Funding acquisition.

Declaration of Competing Interest

The authors report no declarations of interest.

Acknowledgements

This material is based upon work supported by the National Science Foundation under Grant No. 1538125 (Jia, Grejtak, Cunniffe, Shi, Vermaak and Krick). This material is based upon work supported by the National Science Foundation under Grant No. 1826251 (Grejtak and Krick). This material is based, in part, upon work supported by the National Science Foundation under Grant No. 1825815 and No. 1825437 (Compton and Vermaak). This material is based upon work supported by the National Science Foundation Graduate Research Fellowship Program under Grant #1842163 (Babuska). We also want to acknowledge support from AFOSR award # FA9550-18-1-0363 (Krick and Grejtak). Compton and Pack would like to acknowledge support from Honeywell Federal Manufacturing & Technologies through contract DE-NA0002839, administered by Dr. Jamie Messman, Mr. Steven Patterson, and Dr. Eric Eastwood. SiC microfibers were generously provided by Mr. Kevin Fox at Haydale Technologies, Inc.

References

 S. Demiroglu, V. Singaravelu, M.Ö. Seydibeyoğlu, M. Misra, A.K. Mohanty, The use of nanotechnology for fibre-reinforced polymer composites, Fiber Technology for

- Fiber-Reinforced Composites, Elsevier, 2017, pp. 277–297, https://doi.org/10.1016/B978-0-08-101871-2.00013-8.
- [2] V.K. Thakur, M.K. Thakur, Processing and characterization of natural cellulose fibers/thermoset polymer composites, Carbohydr. Polym. 109 (2014) 102–117, https://doi.org/10.1016/j.carbpol.2014.03.039.
- [3] L. Mohammed, M.N.M. Ansari, G. Pua, M. Jawaid, M.S. Islam, A review on natural Fiber reinforced polymer composite and its applications, Int. J. Polym. Sci. 2015 (2015), https://doi.org/10.1155/2015/243947.
- [4] R. Ramasubramaniam, J. Chen, H. Liu, Homogeneous carbon nanotube/polymer composites for electrical applications, Appl. Phys. Lett. 83 (2003) 2928–2930, https://doi.org/10.1063/1.1616976.
- [5] V.K. Thakur, M.K. Thakur, P. Raghavan, M.R. Kessler, Progress in green polymer composites from lignin for multifunctional applications: a review, ACS Sustain. Chem. Eng. 2 (2014) 1072–1092, https://doi.org/10.1021/sc500087z.
- [6] T.P. Sathishkumar, S. Satheeshkumar, J. Naveen, Glass fiber-reinforced polymer composites - a review, J. Reinf. Plast. Compos. 33 (2014) 1258–1275, https://doi. org/10.1177/0731684414530790.
- [7] F.A. López, M.I. Martín, F.J. Alguacil, J.M. Rincón, T.A. Centeno, M. Romero, Thermolysis of fibreglass polyester composite and reutilisation of the glass fibre residue to obtain a glass-ceramic material, J. Anal. Appl. Pyrolysis 93 (2012) 104–112, https://doi.org/10.1016/j.jaap.2011.10.003.
- [8] V. Dhand, G. Mittal, K.Y. Rhee, S.J. Park, D. Hui, A short review on basalt fiber reinforced polymer composites, Compos. Part B Eng. 73 (2015) 166–180, https://doi.org/10.1016/j.compositesb.2014.12.011.
- [9] B.A. Krick, J.J. Ewin, E.J. McCumiskey, Tribofilm formation and run-in behavior in ultra-low-wearing polytetrafluoroethylene (PTFE) and alumina nanocomposites, Tribol. Trans. 57 (2014) 1058–1065, https://doi.org/10.1080/10402004.2014. 933934.
- [10] B.A. Krick, J.J. Ewin, G.S. Blackman, C.P. Junk, W. Gregory Sawyer, Environmental dependence of ultra-low wear behavior of polytetrafluoroethylene (PTFE) and alumina composites suggests tribochemical mechanisms, Tribol. Int. 51 (2012) 42–46, https://doi.org/10.1016/j.triboint.2012.02.015.
- [11] J.R. Potts, D.R. Dreyer, C.W. Bielawski, R.S. Ruoff, Graphene-based polymer nanocomposites, Polymer (Guildf) 52 (2011) 5–25, https://doi.org/10.1016/j. polymer.2010.11.042.
- [12] M.Z. Rong, M.Q. Zhang, W.H. Ruan, Surface modification of nanoscale fillers for improving properties of polymer nanocomposites: a review, Mater. Sci. Technol. 22 (2006) 787–796, https://doi.org/10.1179/174328406X101247.
- [13] W.L. Song, W. Wang, L.M. Veca, C.Y. Kong, M.S. Cao, P. Wang, M.J. Meziani, H. Qian, G.E. Lecroy, L. Cao, Y.P. Sun, Polymer/carbon nanocomposites for enhanced thermal transport properties - Carbon nanotubes versus graphene sheets as nanoscale fillers, J. Mater. Chem. 22 (2012) 17133–17139, https://doi.org/10.1039/c2im32469e.
- [14] R.R. Collino, T.R. Ray, R.C. Fleming, J.D. Cornell, B.G. Compton, M.R. Begley, Deposition of ordered two-phase materials using microfluidic print nozzles with acoustic focusing, Extrem. Mech. Lett. 8 (2016) 96–106, https://doi.org/10.1016/j. eml.2016.04.003.
- [15] B.G. Compton, J.W. Kemp, T.V. Novikov, R.C. Pack, C.I. Nlebedim, C.E. Duty, O. Rios, M.P. Paranthaman, Direct-write 3D printing of NdFeB bonded magnets, Mater. Manuf. Process. 33 (2018) 109–113, https://doi.org/10.1080/10426914. 2016.1221097.
- [16] S. Malek, J.R. Raney, J.A. Lewis, L.J. Gibson, Lightweight 3D cellular composites inspired by balsa, Bioinspir. Biomim. 12 (2017), https://doi.org/10.1088/1748-3190/aa6028.
- [17] L. Friedrich, R. Collino, T. Ray, M. Begley, Acoustic control of microstructures during direct ink writing of two-phase materials, Sens. Actuators A Phys. 268 (2017) 213–221, https://doi.org/10.1016/j.sna.2017.06.016.
- [18] J.P. Lewicki, J.N. Rodriguez, C. Zhu, M.A. Worsley, A.S. Wu, Y. Kanarska, J.D. Horn, E.B. Duoss, J.M. Ortega, W. Elmer, R. Hensleigh, R.A. Fellini, M.J. King, 3D-printing of meso-structurally ordered carbon fiber/polymer composites with unprecedented orthotropic physical properties, Sci. Rep. 7 (2017) 1–14, https://doi. org/10.1038/srep43401.
- [19] J.R. Raney, B.G. Compton, J. Mueller, T.J. Ober, K. Shea, J.A. Lewis, Rotational 3D printing of damage-tolerant composites with programmable mechanics, Proc. Natl. Acad. Sci. U. S. A. 115 (2018) 1198–1203, https://doi.org/10.1073/pnas. 1715157115
- [20] B.G. Compton, N.S. Hmeidat, R.C. Pack, M.F. Heres, J.R. Sangoro, Electrical and mechanical properties of 3D-Printed graphene-reinforced epoxy, JOM 70 (2018) 292–297, https://doi.org/10.1007/s11837-017-2707-x.
- [21] P. Parandoush, D. Lin, A review on additive manufacturing of polymer-fiber composites, Compos. Struct. 182 (2017) 36–53, https://doi.org/10.1016/j.compstruct. 2017.08.088.
- [22] T.D. Ngo, A. Kashani, G. Imbalzano, K.T.Q. Nguyen, D. Hui, Additive manufacturing (3D printing): a review of materials, methods, applications and challenges, Compos. Part B Eng. 143 (2018) 172–196, https://doi.org/10.1016/j.compositesb.2018.02. 012.
- [23] J. Kiendl, C. Gao, Controlling toughness and strength of FDM 3D-printed PLA components through the raster layup, Compos. Part B Eng. 180 (2020) 107562, https://doi.org/10.1016/j.compositesb.2019.107562.
- [24] G.B. Jeffery, The motion of ellipsoidal particles immersed in a viscous fluid, Proc. R. Soc. London. Ser. A, Contain. Pap. a Math. Phys. Character. 102 (1922) 161–179, https://doi.org/10.1098/rspa.1922.0078.
- [25] F. Folgar, C.L. Tucker, Orientation Behavior of Fibers in Concentrated Suspensions, J. Reinf. Plast. Compos. 3 (1984) 98–119, https://doi.org/10.1177/ 073168448400300201.
- [26] S.G. Advani, C.L. Tucker, The use of tensors to describe and predict Fiber

- orientation in short Fiber composites, J. Rheol. (N. Y. N. Y) 31 (1987) 751–784, https://doi.org/10.1122/1.549945.
- [27] S.G. Advani, C.L. Tucker, A numerical simulation of short fiber orientation in compression molding, Polym. Compos. 11 (1990) 164–173, https://doi.org/10. 1002/pc.750110305.
- [28] M. Gupta, K.K. Wang, Fiber orientation and mechanical properties of short-fiber-reinforced injection-molded composites: simulated and experimental results, Polym. Compos. 14 (1993) 367–382, https://doi.org/10.1002/pc.750140503.
- [29] D.A. Jack, D.E. Smith, Elastic properties of short-fiber polymer composites, derivation and demonstration of analytical forms for expectation and variance from orientation tensors, J. Compos. Mater. 42 (2008) 277–308, https://doi.org/10.1177/0021998307086388.
- [30] B.P. Heller, D.E. Smith, D.A. Jack, Effects of extrudate swell and nozzle geometry on fiber orientation in Fused Filament Fabrication nozzle flow, Addit. Manuf. 12 (2016) 252–264, https://doi.org/10.1016/j.addma.2016.06.005.
- [31] M.L. Shofner, K. Lozano, F.J. Rodríguez-Macías, E.V. Barrera, Nanofiber-reinforced polymers prepared by fused deposition modeling, J. Appl. Polym. Sci. 89 (2003) 3081–3090, https://doi.org/10.1002/app.12496.
- [32] H.L. Tekinalp, V. Kunc, G.M. Velez-Garcia, C.E. Duty, L.J. Love, A.K. Naskar, C.A. Blue, S. Ozcan, Highly oriented carbon fiber–polymer composites via additive manufacturing, Compos. Sci. Technol. 105 (2014) 144–150, https://doi.org/10. 1016/j.compscitech.2014.10.009.
- [33] A.S. Gladman, E.A. Matsumoto, R.G. Nuzzo, L. Mahadevan, J.A. Lewis, Biomimetic 4D printing, Nat. Mater. 15 (2016) 413–418, https://doi.org/10.1038/NMAT4544.
- [34] B.G. Compton, J.A. Lewis, 3D-printing of lightweight cellular composites, Adv. Mater. 26 (2014) 5930–5935, https://doi.org/10.1002/adma.201401804.
- [35] N.S. Hmeidat, J.W. Kemp, B.G. Compton, High-strength epoxy nanocomposites for 3D printing, Compos. Sci. Technol. 160 (2018) 9–20, https://doi.org/10.1016/j. compscitech.2018.03.008.
- [36] J. Peng, T.L. Lin, P. Calvert, Orientation effects in freeformed short-fiber composites, Compos. Part A Appl. Sci. Manuf. 30 (1999) 133–138, https://doi.org/10.1016/S1359-835X(98)00110-9.
- [37] T.P. Mohan, M.R. Kumar, R. Velmurugan, Rheology and curing characteristics of epoxy-clay nanocomposites, Polym. Int. 54 (2005) 1653–1659, https://doi.org/10. 1002/pi.1897.
- [38] J.H. Park, S.C. Jana, Mechanism of exfoliation of nanoclay particles in epoxy-clay nanocomposites, Macromolecules 36 (2003) 2758–2768, https://doi.org/10.1021/ ma021509c.
- [39] S. Saber-Samandari, A.A. Khatibi, D. Basic, An experimental study on clay/epoxy nanocomposites produced in a centrifuge, Compos. Part B Eng. 38 (2007) 102–107, https://doi.org/10.1016/j.compositesb.2006.03.010.
- [40] M. Chan, K. Lau, T. Wong, M. Ho, D. Hui, Mechanism of reinforcement in a nanoclay/polymer composite, Compos. Part B Eng. 42 (2011) 1708–1712, https://doi. org/10.1016/i.compositesb.2011.03.011.
- [41] A.A. Azeez, K.Y. Rhee, S.J. Park, D. Hui, Epoxy clay nanocomposites Processing, properties and applications: a review, Compos. Part B Eng. 45 (2013) 308–320, https://doi.org/10.1016/j.compositesb.2012.04.012.
- [42] T. Lan, T.J. Pinnavaia, Clay-reinforced epoxy nanocomposites, Chem. Mater. 6 (1994) 2216–2219. https://doi.org/10.1021/cm00048a006.
- [43] N.S. Hmeidat, R.C. Pack, S.J. Talley, R.B. Moore, B.G. Compton, Mechanical anisotropy in polymer composites produced by material extrusion additive manufacturing, Addit. Manuf. 34 (2020) 101385, https://doi.org/10.1016/j.addma.

- 2020.101385.
- [44] U. Nirmal, B.F. Yousif, D. Rilling, P.V. Brevern, Effect of betelnut fibres treatment and contact conditions on adhesive wear and frictional performance of polyester composites, Wear 268 (2010) 1354–1370, https://doi.org/10.1016/j.wear.2010. 02.004.
- [45] C.W. Chin, B.F. Yousif, Potential of kenaf fibres as reinforcement for tribological applications, Wear 267 (2009) 1550–1557, https://doi.org/10.1016/j.wear.2009. 06.002.
- [46] N. Chand, U.K. Dwivedi, Influence of Fiber orientation on high stress wear behavior of sisal fiber-reinforced epoxy composites, Polym. Compos. 37 (2016) 915–924, https://doi.org/10.1002/pc.
- [47] N.-H. Sung, N.P. Suh, Effect of fiber orientation on friction and wear of fiber reinforced polymeric composites, Wear 53 (1979) 129–141, https://doi.org/10.1016/ 0043_1648(79)90224_2
- [48] B.F. Yousif, N.S.M. El-Tayeb, Tribological evaluations of polyester composites considering three orientations of CSM glass fibres using BOR machine, Appl. Compos. Mater. 14 (2007) 105–116, https://doi.org/10.1007/s10443-007-9034
- [49] G. Zhang, Z. Rasheva, A.K. Schlarb, Friction and wear variations of short carbon fiber (SCF)/PTFE/graphite (10 vol.%) filled PEEK: effects of fiber orientation and nominal contact pressure, Wear 268 (2010) 893–899, https://doi.org/10.1016/j. wear.2009.12.001.
- [50] T.L. Schmitz, J.E. Action, D.L. Burris, J.C. Ziegert, W.G. Sawyer, Wear-rate uncertainty analysis, J. Tribol. 126 (2004) 802, https://doi.org/10.1115/1.1792675.
- [51] C.C. Battaile, D.J. Srolovitz, Kinetic monte carlo simulation of chemical vapor deposition, Annu. Rev. Mater. Res. 32 (2002) 297–319, https://doi.org/10.1146/annurev.matsci.32.012102.110247.
- [52] A. Chatterjee, D.G. Vlachos, An overview of spatial microscopic and accelerated kinetic Monte Carlo methods, J. Comput. Mater. Des. 14 (2007) 253–308, https://doi.org/10.1007/s10820-006-9042-9.
- [53] D.L. Burris, W.G. Sawyer, Addressing practical challenges of low friction coefficient measurements, Tribol. Lett. 35 (2009) 17–23, https://doi.org/10.1007/s11249-009.9438-2
- [54] G.M. Erickson, M.A. Sidebottom, J.F. Curry, D.I. Kay, S. Kuhn-Hendricks, M.A. Norell, W.G. Sawyer, B.A. Krick, Paleo-tribology: Development of wear measurement techniques and a three-dimensional model revealing how grinding dentitions selfwear to enable functionality, Surf. Topogr. Metrol. Prop. 4 (2016), https://doi.org/10.1088/2051-672X/4/2/024001.
- [55] E.A. Sander, V.H. Barocas, Comparison of 2D fiber network orientation measurement methods, J. Biomed. Mater. Res. - Part A. 88 (2009) 322–331, https://doi.org/ 10.1002/jbm.a.31847.
- [56] N. Chand, M. Fahim, Role of polymeric matrices in improving wear resistance of irradiated FRP composites, Tribol. Lett. 1 (1995) 301–307, https://doi.org/10. 1007/BF00174256.
- [57] N.P. Suh, An overview of the delamination theory of wear, Wear 44 (1977) 1–16, https://doi.org/10.1016/0043-1648(77)90081-3.
- [58] A.G. Evans, J.W. Hutchinson, The mechanics of coating delamination in thermal gradients, Surf. Coatings Technol. 201 (2007) 7905–7916, https://doi.org/10. 1016/j.surfcoat 2007 03 029
- [59] J.W. Kemp, N.S. Hmeidat, B.G. Compton, Boron nitride-reinforced polysilazanederived ceramic composites via direct-ink writing, J. Am. Ceram. Soc. (2020) 1–8, https://doi.org/10.1111/jace.17084.